Journal of Nuclear Materials 531 (2020) 152018

Contents lists available at ScienceDirect

Journal of Nuclear Materials

journal homepage: www.elsevier.com/locate/jnucmat

# Significant growth of vacancy-type defects by post-irradiation annealing in neon ion-irradiated tungsten probed by a slow positron beam

A. Yabuuchi *, M. Tanaka , A. Kinomura

*Institute for Integrated Radiation and Nuclear Science, Kyoto University, Kumatori, Osaka, 590-0494, Japan*

ARTICLE INFO

*Article history:*
Received 24 July 2019
Received in revised form
4 December 2019
Accepted 20 January 2020
Available online 23 January 2020

*Keywords:*
Tungsten
Noble gas
Ion irradiation
Vacancy
Positron annihilation spectroscopy
Slow positron beam

ABSTRACT

Irradiation damage and its evolution in noble gas ion-irradiated tungsten have not been investigated in detail other than in the case of helium ion irradiation. In this study, irradiation-induced vacancy-type defects in helium ion- and neon ion-irradiated tungsten were investigated by using a slow positron beam, and their annealing behavior in the temperature range of 20°C-900°C was compared by characterizing the Doppler broadening of positron annihilation radiation spectra. In helium ion-irradiated tungsten, slight aggregation of irradiation-induced vacancy-type defects was observed upon annealing, but eventually, a large portion of the vacancy clusters was eliminated after annealing at 900°C. In contrast, in neon ion-irradiated tungsten, irradiation-induced vacancy-type defects were observed to aggregate significantly at 300°C and 600°C. In addition, the large vacancy clusters formed by the aggregation survived even after annealing at 900°C.



## 1. Introduction

Since tungsten (W) is expected to be a plasma-facing wall material for fusion reactors [1–4], irradiation damage to tungsten induced by protons or helium ion-irradiation ($He^+$-irradiation) has been widely studied. Recently, intentional injection of neon (Ne) and/or argon (Ar) gases into the fusion plasma were studied to decrease the heat load on the tungsten wall [5–7]. In addition, noble gas plasma irradiation has been known to form fuzz-like nanostructures on the tungsten surface [8], which is considered to be related to the aggregation of vacancies and/or gas atoms. The fuzz-like nanostructures have been reported to be not formed by Ne or Ar plasma exposure even under the irradiation condition where the nanostructures are readily formed by He plasma irradiation [9]. Thus, it is necessary to understand irradiation defects formed by irradiating noble gases into tungsten.

Positron annihilation spectroscopy is a powerful probe for investigating vacancy-type defects in crystalline materials [10–12], and several defect studies in proton- or $He^+$-irradiated tungsten have been performed using positrons [13–16]. However, few studies on the defects in noble gas ion-irradiated tungsten using positrons have been reported [17,18], except for $He^+$-irradiation. Irradiation of the other noble gases which represent heavier particles can cause more significant damage to tungsten. In addition, the annealing behavior of irradiation-induced defects may also be different because the binding energies between vacancy ($V$) and gas atom in $V$–Ne or $V$–Ar are much larger than that in $V$–He [19]. The difference in defect structure will also affect the tritium retention capability of tungsten. In this study, the annealing behavior of vacancy-type defects in $He^+$ and $Ne^+$-irradiated tungsten was probed using a slow positron beam.

## 2. Experimental method

High-purity sintered tungsten samples (99.999%) were cut into $15 \times 15 \times 0.8$ $mm^3$ pieces. After mechanical and electrochemical polishing, all samples were annealed in vacuum for 15 min at approximately 2200°C by using an electron-bombardment heating technique [20] to eliminate initial defects. The annealed tungsten samples were irradiated with helium or neon ions with an energy of 50 keV. The total irradiation doses of $He^+$ and $Ne^+$ were $2.5 \times 10^{16}$ $He^+/cm^2$ and $4.2 \times 10^{15}$ $Ne^+/cm^2$, respectively. The

* Corresponding author.
*E-mail address:* yabuuchi@rri.kyoto-u.ac.jp (A. Yabuuchi).

https://doi.org/10.1016/j.jnucmat.2020.152018
0022-3115/

irradiation energy of the ion beams (50 keV) is the maximum energy of the ion implanter used in this study. In order to make the projected range of $He^+$ the same as that of 50 keV $Ne^+$, $He^+$ must be irradiated at about 10 keV. However, it was difficult for the ion implanter to extract 10 keV ions with sufficient beam current. Thus, both ion species were irradiated at 50 keV. The irradiation dose of $He^+$ was increased to make the concentration of the implanted gas atoms comparable since the projected range of $He^+$ is deeper than that of $Ne^+$ for the same irradiation energy. The original experimental design was intended to make the He and Ne atom concentrations equal in the positron-probed region of both samples. However, due to an unintentional error in calculating the irradiation conditions, the concentration of implanted gas atoms in both samples differed by two times as described later. The ion beam flux was approximately $7 \times 10^{12}$ ions/cm•2s for both $He^+$ and $Ne^+$, and the sample during irradiation was kept at room temperature.

The ion and vacancy distributions in tungsten were calculated with a displacement threshold energy of 90 eV [17,21] using the SRIM-2013 code [22,23]. The incident positron distributions $P(z)$ were calculated by using a formula called the Makhovian distribution [24],

$$P(z) = \frac{mz^{m-1}}{z_0^m} \exp\left[ -\left(\frac{z}{z_0}\right)^m \right], \tag{1}$$

$$z_0 = \frac{\bar{z}}{\Gamma\left[\left(\frac{1}{m}\right)+1\right]}, \tag{2}$$

$$\bar{z} = \frac{AE^n}{\rho}, \tag{3}$$

where $z$, ρ, and $E$ are the depth in nm, target density in g/cm$^3$, and incident positron energy in keV, respectively. $A$ is a constant, and the unit of $A/\rho$ is nm/keV$^n$. The mean positron implantation depth in nm is denoted by $\bar{z}$. In this study, calculations were carried out for $A = 40$, $m = 1.9$, and $n = 1.6$.

The samples irradiated with $He^+$ or $Ne^+$ and an unirradiated sample were probed by a reactor-based slow positron beam constructed at Kyoto University Research Reactor (KUR) [25–28], and the Doppler broadening of annihilation radiation (DBAR) spectra were acquired using a high-purity germanium detector. The energy of the positron annihilation radiation reflects the momentum of the annihilated electron and is Doppler-shifted from 511 keV. Thus, the shape of its spectrum becomes broad. However, when positrons are trapped at vacancy-type defects, the fraction of positrons annihilated with valence electrons increases. Since the momentum of the valence electrons is lower than that of the core electrons, the shape of the DBAR spectrum becomes sharp when positrons are trapped at vacancy-type defects. The shape of the acquired DBAR spectra was characterized in terms of $S$- and $W$-parameters, corresponding to the annihilation with low and high momentum electrons, respectively. $S$ ($W$) was defined as the number of annihilation events over the energy range of 510.23–511.77 keV (501.71–507.90 keV and 514.10–520.29 keV) divided by the total number of events in the energy range of 501.71–520.29 keV. The observed $S$- and $W$-parameters are given by

$$S = \frac{\lambda_f}{\lambda_f + \kappa_d} S_f + \frac{\kappa_d}{\lambda_f + \kappa_d} S_d, \tag{4}$$

$$W = \frac{\lambda_f}{\lambda_f + \kappa_d} W_f + \frac{\kappa_d}{\lambda_f + \kappa_d} W_d, \tag{5}$$

where $\lambda_f$ and $\kappa_d$ are the positron annihilation rate of free-state positrons (*i.e.*, delocalized positrons) and the positron trapping rate into defects, respectively. The $\kappa_d/(\lambda_f + \kappa_d)$ denotes the fraction of positrons trapped at defects, and $S_f$ ($W_f$) and $S_d$ ($W_d$) are $S$-parameters ($W$-parameters) given by free-state positrons and defect-trapped positrons, respectively. The values of $S$ and $W$ increase and decrease, respectively, when positrons are trapped at vacancy-type defects. Vacancy-type defects having different sizes give unique $S_d$ and $W_d$ values depending on the defect size. Thus, Eqs. (4) and (5) indicate that $S$ and $W$ depend on both the defect size and the defect concentration. In this study, the DBAR spectra were acquired with positron energies of 20 keV, 8.5 keV, and 6 keV for unirradiated, $He^+$-irradiated, and $Ne^+$-irradiated samples, respectively. All the $S$- and $W$-parameters were normalized to those obtained from the unirradiated sample probed with positron energy of 20 keV. For the same defect species, the $S$–$W$ correlations are plotted on the same straight line regardless of the defect concentration. In this study, the $S$- and $W$-parameters obtained from the unirradiated (defect-free) sample probed with positron energy of 20 keV were defined as $S_f$ and $W_f$, respectively.

For the unirradiated sample, the DBAR spectra were also acquired by varying the incident positron energy in the range of 1–30 keV. In the incident positron energy dependence measurement of the unirradiated sample, the DBAR spectra were acquired with about $6 \times 10^4$ total events at each positron energy. The irradiated samples were annealed for 15 min in vacuum at a temperature range of 200°C-900°C after measuring the as-irradiated state. The DBAR spectra were acquired after annealing at each temperature. About $6 \times 10^6$ total events were acquired for the DBAR spectra in the unirradiated, $He^+$-irradiated, and $Ne^+$-irradiated samples measured at 20 keV, 8.5 keV, and 6 keV, respectively. Details will be described in the next section, actually, the $He^+$-irradiated sample prepared in this study should have been probed with a 15 keV positron beam. However, there was an unintended error in the calculation of irradiation conditions, which was noticed after the positron annihilation and annealing experiments. Thus, in this study, the $He^+$-irradiated sample was probed with non-optimal energy positrons (8.5 keV) determined based on the miscalculated $He^+$ implantation profile. After the positron annihilation experiments, the implantation profiles were recalculated, and the experimental results were interpreted based on the correct implantation profiles.

## 3. Results and discussion

Fig. 1 shows the calculated ion, displacement per atom (DPA), and positron distributions.

The ion and DPA distributions were calculated by using the SRIM code. Sputtering of the target by the ion irradiation is negligible in the distributions. Positron distributions for the $He^+$- and $Ne^+$-irradiated samples are calculated with positron energies of 8.5 keV and 6 keV, respectively. For the $Ne^+$-irradiated sample, the incident distribution of 6 keV positrons almost agrees with the $Ne^+$ implantation distribution. For the $He^+$-irradiated sample, the incident distribution of 8.5 keV positrons unintentionally deviates from the $He^+$ implantation distribution. From the correct recalculated result of the $He^+$ implantation profile performed after the positron annihilation experiments, a positron incident profile was confirmed to almost agree with the $He^+$ implantation profile when a 15 keV positron beam was used. However, the $He^+$-irradiated sample prepared in this study was probed by a positron beam with a non-optimal energy of 8.5 keV.

The ratio of implanted ions to tungsten atoms and the DPA for the $He^+$- and $Ne^+$-irradiated samples are summarized in Table 1.

These values were calculated by weighted averaging based on 8.5 keV or 6 keV positron distributions shown in Fig. 1, *i.e.*, the

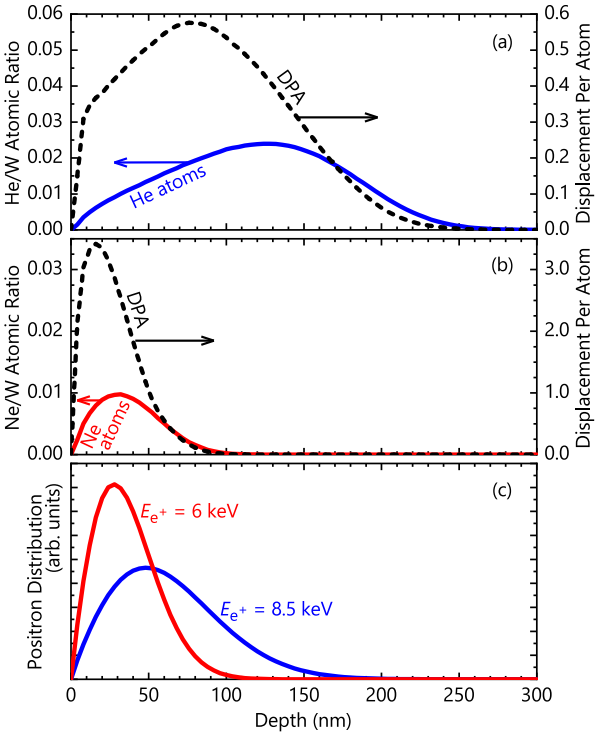


**Fig. 1.** (a), (b) He or Ne atom distribution (solid line) and DPA distribution (dashed line) upon irradiation with 50 keV ion beam into tungsten. (c) Stopping profiles of 8.5 keV and 6 keV positrons which probed the $He^+$- and $Ne^+$-irradiated samples, respectively.

**Table 1**
Irradiation dose of each ion, the ratio of implanted ions to tungsten atoms, and DPA, for the $He^+$- and $Ne^+$-irradiated tungsten samples. The implanted ion ratio and the DPA for the $He^+$- and $Ne^+$-irradiated tungsten samples were calculated by weighted averaging based on 8.5 keV and 6 keV positron distributions shown in Fig. 1, respectively.

| Irradiated Ion Species | $He^+$ | $Ne^+$ |
|---|---|---|
| Irradiation Dose (ions/cm$^2$) | $2.5 \times 10^{16}$ | $4.2 \times 10^{15}$ |
| Ratio of Ions/W-Atoms | $1.5 \times 10^{-2}$ | $7.5 \times 10^{-3}$ |
| Displacement Per Atom | $4.9 \times 10^{-1}$ | $2.1 \times 10^{0}$ |

average in the range probed by positrons. While the average ratio of implanted ions to tungsten atoms in the $Ne^+$-irradiated sample was half that of the $He^+$-irradiated sample, the average DPA of the $Ne^+$-irradiated sample was derived to be more than four times that of the $He^+$-irradiated sample, according to SRIM calculations. However, most of the initially-formed Frenkel pairs annihilate due to recombination. In the case of ion irradiation into tungsten, the number of residual Frenkel pairs that eventually survive is reported to become around 0.2 times that of the initially-formed Frenkel pairs when the energy of the primary knock-on atoms (PKA) exceeds 10 keV [29,30].

Fig. 2 shows normalized *S*-parameters for the unirradiated sample as a function of incident positron energy.

In the sample annealed at 2200°C, only the positron lifetime of 104 ps was detected, corresponding to the positron lifetime of the defect-free tungsten lattice [27]. For incident positron energy over 20 keV, the *S*-parameters reach a nearly constant value, which corresponds to the intrinsic *S*-parameter of the sample. By contrast, at incident positron energies below 20 keV, the *S*-parameter increases with decreasing positron energy, which is attributable to positron annihilation events at the surface being mixed in the DBAR

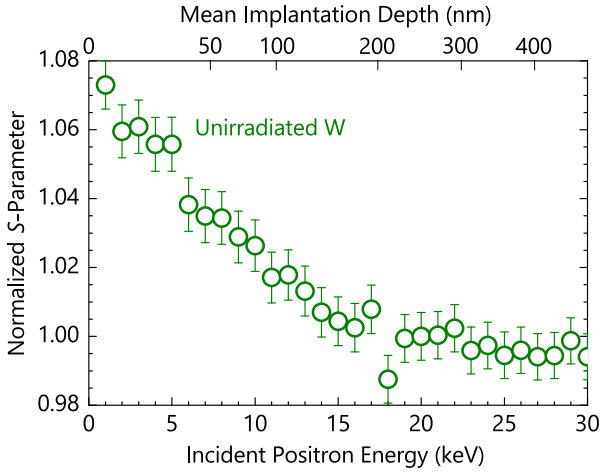


**Fig. 2.** *S*-parameters as a function of incident positron energy obtained from the unirradiated sample. All *S*-parameters are normalized to that obtained with positron energy of 20 keV. The upper horizontal axis denotes the mean positron implantation depth corresponding to the incident positron energy.

spectra since positrons stop at a depth at which they can diffuse back to the surface. Since the positron diffusion length becomes longer in annealed, defect-free samples, the surface effect appears in the DBAR spectrum until the incident positron energy reaches nearly 20 keV.

Fig. 3 shows *S*–*W* correlations for the $He^+$- and $Ne^+$-irradiated samples after annealing at each temperature and those for the unirradiated sample probed with positron energies of 1–10 keV.

The $(S, W) = (1, 1)$ point shown in Fig. 3 represents the values for the unirradiated sample probed with positron energy of 20 keV, thus corresponding to *S*- and *W*-parameters given by free-state positrons (*i.e.*, positron annihilation in a defect-free lattice). The observed *S* and *W* vary depending on the fraction of positrons trapped at defects, but those are given by the linear combination of $S_f$-$S_d$ or $W_f$-$W_d$ as shown in Eqs. (4) and (5), respectively. Therefore, when only one defect species is present, *S*–*W* correlations are plotted in the same straight line regardless of the defect concentration.

In the unirradiated sample, a portion of the positrons annihilates at the surface when the positrons are implanted with energies of 1–10 keV, as shown in Fig. 2. The *S* and *W* show maximum and minimum values, respectively, because the fraction of positrons annihilating at the surface is highest when positrons are implanted with an energy of 1 keV; however, *S*–*W* correlations obtained from the unirradiated sample probed with positron energies of 1–10 keV are plotted on almost the same straight line except for the 5 keV data. That is, the straight line having this slope $D_0$ corresponds to positron annihilation at the surface.

In the case of the irradiated samples, the *S*–*W* correlations for both samples are plotted on the same straight line having the slope $D_1$, in the as-irradiated state; *i.e.*, defect species (defect size) contained in both samples are the same or similar at the initial stage. The plot of the $Ne^+$-irradiated sample being located lower right that of the $He^+$-irradiated one in the as-irradiated state means that the $Ne^+$-irradiated sample has a higher defect concentration than the $He^+$-irradiated one; this is also consistent with the SRIM calculations shown in Table 1. The *S*–*W* correlations of the $He^+$-irradiated sample deviate slightly toward larger *S* values than the $D_1$ straight line upon annealing. Eventually, the *S*–*W* is plotted on the $D_0$ straight line after annealing at 900°C. This shows that irradiation-induced vacancy-type defects aggregate, but eventually, a large part of those defects are annealed out. By contrast, *S*–*W*

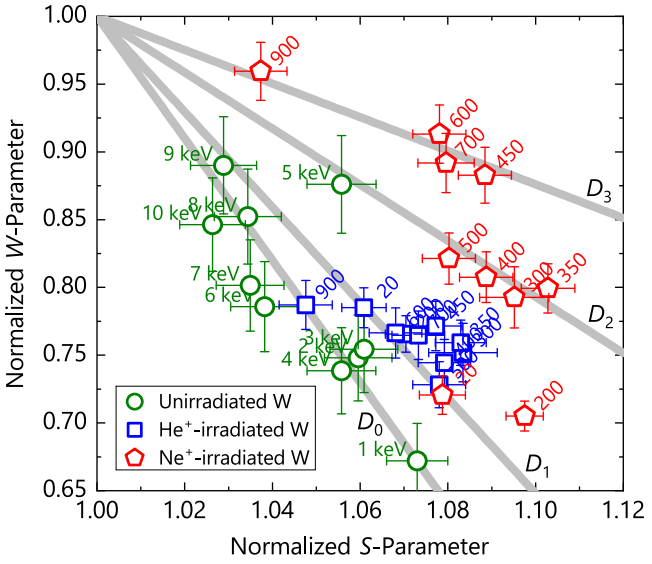


**Fig. 3.** *S*–*W* correlations obtained from the $He^+$- and $Ne^+$-irradiated samples measured after annealing at each temperature. The numbers in the upper right of each plot indicate the annealing temperature in °C. The $(S, W) = (1, 1)$ point indicates the values obtained from the unirradiated sample probed with positron energy of 20 keV, *i.e.*, the values corresponding to positron annihilation in a defect-free lattice. *S*–*W* plots obtained from the unirradiated sample probed with positron energies of 1–10 keV, including the positron annihilation component at the surface, are depicted as open circles. Four straight lines having representative slopes $D_0$–$D_3$ are also depicted in light gray.

correlations of the $Ne^+$-irradiated sample, for which the as-irradiated state is plotted on the same straight line as that of the $He^+$-irradiated one, are plotted on other straight lines having different slopes with increasing annealing temperature. The *S*–*W* correlations for the $Ne^+$-irradiated sample are plotted on the $D_2$ and $D_3$ straight lines after annealing at 300°C and 600°C, respectively. This deviation of the *S*–*W* correlations indicates that the vacancy-type defects in the $Ne^+$-irradiated sample aggregate and become larger vacancy clusters at 300°C and 600°C [15]. After annealing at 900°C, the *S*–*W* correlation of the $Ne^+$-irradiated sample is plotted on the $D_3$ straight line, thus indicating that the larger vacancy clusters still survive.

When irradiating particles having a mass of $m_1$ to the target with an energy of $E_1$, the maximum energy $E_{p,max}$ of PKA is given by

$$E_{p,max} = \frac{4m_1m_2}{(m_1+m_2)^2}E_1, \tag{6}$$

where $m_2$ is the mass of the target atom [31]. Based on Eq. (6), the $E_{p,max}$ for the $He^+$- and $Ne^+$-irradiated samples are calculated to be 4.2 keV and 17.8 keV, respectively. Thus, the size of each cascade and the number of vacancy-type defects contained therein are expected to be larger in the $Ne^+$-irradiated sample than in the $He^+$-irradiated one. Even in large collision cascades, the DBAR spectra reflect the size of the individual vacancy-type defects contained in the cascades, as a result, a similar size of vacancy-type defects was detected from both as-irradiated samples. Past radiation damage studies based on molecular dynamics simulations have reported that irradiation-induced vacancy-type defects in tungsten tend to remain isolated without being clustered [29,30].

One possible factor of the significant growth of vacancy-type defects by annealing observed in the $Ne^+$-irradiated sample is speculated to be the difference in the size of the collision cascades formed in both samples. The size of the cascade formed in the $Ne^+$-irradiated sample is larger than that formed in the $He^+$-irradiated one. A large number of vacancy-type defects contained in the large cascade developed into large vacancy clusters during annealing, and as a result, they survived even after annealing at 900°C. In contrast, from the small cascade formed in the He-irradiated sample, only relatively small vacancy clusters were formed during annealing and eventually annealed out at 900°C.

Other possible factors are the difference in the DPA or the difference in the concentration of the implanted noble gas atoms. As shown in Table 1, in the positron-probed region, the $Ne^+$-irradiated sample was irradiated with four times higher DPA compared with the $He^+$-irradiated one. The highly-concentrated vacancy-type defects may have led to differences in their clustering behavior. On the other hand, the noble gas atom concentration of the $He^+$-irradiated sample in the positron-probed region was twice higher than that of the $Ne^+$-irradiated one. The binding energy between monovacancy in tungsten and He or Ne atom has been reported to be considerably large (~4.7 eV for *V*–He and ~8.5 eV for *V*–Ne) [19]. Such a difference in the concentration of impurity atoms that strongly bind to vacancies may also affect the clustering behavior of vacancy-type defects during annealing.

To clarify the factors that caused the difference in clustering behavior of vacancy-type defects observed in the He- and Ne-irradiated samples, further investigations are desired by using samples with the same DPA or the same concentration of noble gas atoms. However, the residual efficiency of the Frenkel pairs has been reported to be greatly dependent on PKA energy, especially in the energy region where the PKA energy is below 10 keV [29,30]. Therefore, it may be necessary to prepare samples with the same residual Frenkel pair concentration in consideration of the difference of residual efficiency, rather than preparing the same DPA samples. In addition, beam-based positron annihilation lifetime measurements will also be helpful to observe the clustering behavior of vacancy-type defects in future studies.

## 4. Conclusion

In this study, $He^+$- and $Ne^+$-irradiated tungsten samples were probed by a slow positron beam after annealing in the temperature range of 20°C-900°C. The annealing behavior of irradiation-induced vacancy-type defects in both samples was observed by characterizing the DBAR spectra with *S*- and *W*-parameters. A slight deviation of the *S*–*W* correlations was observed in the $He^+$-irradiated sample, suggesting the aggregation of vacancy-type defects with increasing annealing temperature. However, eventually, a large portion of these vacancy clusters was eliminated after annealing at 900°C. By contrast, the *S*–*W* correlations of the $Ne^+$-irradiated sample clearly showed that the irradiation-induced vacancy-type defects aggregate and become larger after annealing at 300°C and 600°C. Moreover, it was also shown that the vacancy clusters still survive in the $Ne^+$-irradiated sample after annealing at 900°C. The difference in the clustering behavior may be attributed to differences in the cascade size, the DPA, and the concentration of the implanted noble gas atoms. However, in the present work, the DPA or noble gas atom concentrations in the positron-probed region did not agree between the two prepared samples. To clarify which factor causes the difference in the clustering behavior observed in this work, further studies are necessary, for example investigating samples with the same DPA, the same residual Frenkel pair concentration, or the same noble gas atom concentration.

## Declaration of competing interest

The authors declare that they have no known competing financial interests or personal relationships that could have appeared to influence the work reported in this paper.

## CRediT authorship contribution statement

**A. Yabuuchi:** Conceptualization, Formal analysis, Investigation, Resources, Writing - original draft, Visualization, Supervision, Funding acquisition. **M. Tanaka:** Investigation, Visualization. **A. Kinomura:** Investigation, Writing - review & editing.

## Acknowledgements

The authors would like to thank S. Makimura (KEK) for providing the high-purity tungsten used in this study. We also thank H. Araki, M. Mizuno, and K. Sugita (Osaka Univ.) for their assistance in the sample cutting. We are grateful to T. Yoshiie, H. Shirai, and Y. Kuzuya (Kyoto Univ.) for their help in restoring and improving the ion-implanter used in this study. This work has been performed in part under the joint-use facilities of the Institute for Integrated Radiation and Nuclear Science, Kyoto University. This work was financially supported by Japan Society for the Promotion of Science KAKENHI Grant Number JP17K14896.

## References

[1] H.E. Prebble, C.B.A. Forty, G.J. Butterworth, Potential collector surface materials for divertors, J. Nucl. Mater. 191–194 (1992) 391, https://doi.org/10.1016/S0022-3115(09)80073-1.
[2] V. Philipps, Tungsten as material for plasma-facing components in fusion devices, J. Nucl. Mater. 415 (2011) S2, https://doi.org/10.1016/j.jnucmat.2011.01.110.
[3] M. Rieth, S.L. Dudarev, S.M.G. de Vicente, J. Aktaa, T. Ahlgren, S. Antusch, D.E.J. Armstrong, M. Balden, N. Baluc, M.-F. Barthe, W.W. Basuki, M. Battabyal, C.S. Becquart, D. Blagoeva, H. Boldyryeva, J. Brinkmann, M. Celino, L. Ciupinski, J.B. Correia, A.D. Backer, C. Domain, E. Gaganidze, C. García-Rosales, J. Gibson, M.R. Gilbert, S. Giusepponi, B. Gludovatz, H. Greuner, K. Heinola, T. Höschen, A. Hoffmann, N. Holstein, F. Koch, W. Krauss, H. Li, S. Lindig, J. Linke, C. Linsmeier, P. López-Ruiz, H. Maier, J. Matejicek, T.P. Mishra, M. Muhammed, A. Muñoz, M. Muzyk, K. Nordlund, D. Nguyen-Manh, J. Opschoor, N. Ordás, T. Palacios, G. Pintsuk, R. Pippan, J. Reiser, J. Riesch, S.G. Roberts, L. Romaner, M. Rosiński, M. Sanchez, W. Schulmeyer, H. Traxler, A. Ureña, J.G. van der Laan, L. Veleva, S. Wahlberg, M. Walter, T. Weber, T. Weitkamp, S. Wurster, M.A. Yar, J.H. You, A. Zivelonghi, Recent progress in research on tungsten materials for nuclear fusion applications in Europe, J. Nucl. Mater. 432 (2013) 482, https://doi.org/10.1016/j.jnucmat.2012.08.018.
[4] T. Hirai, S. Panayotis, V. Barabash, C. Amzallag, F. Escourbiac, A. Durocher, M. Merola, J. Linke, T. Loewenhoff, G. Pintsuk, M. Wirtz, I. Uytdenhouwen, Use of tungsten material for the ITER divertor, Nucl. Mater. Energy 9 (2016) 616, https://doi.org/10.1016/j.nme.2016.07.003.
[5] P. Monier-Garbet, P. Andrew, P. Belo, G. Bonheure, Y. Corre, K. Crombe, P. Dumortier, T. Eich, R. Felton, J. Harling, J. Hogan, A. Huber, S. Jachmich, E. Joffrin, H.R. Koslowski, A. Kreter, G. Maddison, G. Matthews, A. Messiaen, M.F. Nave, J. Ongena, V. Parail, M.E. Puiatti, J. Rapp, R. Sartori, J. Stober, M.Z. Tokar, B. Unterberg, M. Valisa, I. Voitsekhovitch, M. von Hellermann, J.-E. contributors, Impurity-seeded ELMy H-modes in JET, with high density and reduced heat load, Nucl. Fusion 45 (2005) 1404, https://doi.org/10.1088/0029-5515/45/11/022.
[6] H. Urano, M. Nakata, N. Aiba, H. Kubo, M. Honda, N. Hayashi, M. Yoshida, Y. Kamada, The JT-60 Team, Roles of argon seeding in energy confinement and pedestal structure in JT-60U, Nucl. Fusion 55 (2015), 033010, https://doi.org/10.1088/0029-5515/55/3/033010.
[7] T. Nakano, T.J.- Team, Comparison of ne and ar seeded radiative divertor plasmas in JT-60U, J. Nucl. Mater. 463 (2015) 555, https://doi.org/10.1016/j.jnucmat.2014.11.127.
[8] S. Takamura, N. Ohno, D. Nishijima, S. Kajita, Formation of nanostructured tungsten with arborescent shape due to helium plasma irradiation, Plasma Fusion Res. 1 (2006), 051, https://doi.org/10.1585/pfr.1.051.
[9] M. Yajima, M. Yamagiwa, S. Kajita, N. Ohno, M. Tokitani, A. Takayama, S. Saito, A.M. Ito, H. Nakamura, N. Yoshida, Comparison of damages on tungsten surface exposed to noble gas plasmas, Plasma Sci. Technol. 15 (2013) 282, https://doi.org/10.1088/1009-0630/15/3/18.
[10] P. Hautojärvi (Ed.), Positrons in Solids: Topics in Current Physics, Springer, Berlin, 1979.
[11] F. Tuomisto, I. Makkonen, Defect identification in semiconductors with positron annihilation: experiment and theory, Rev. Mod. Phys. 85 (2013) 1583, https://doi.org/10.1103/RevModPhys.85.1583.
[12] J. Čížek, Characterization of lattice defects in metallic materials by positronannihilation spectroscopy: a review, J. Mater. Sci. Technol. 34 (2018) 577, https://doi.org/10.1016/j.jmst.2017.11.050.
[13] P.M.G. Nambissan, P. Sen, Positron annihilation studies on alpha irradiated tungsten, Solid State Commun. 71 (1989) 1165, https://doi.org/10.1016/0038-1098(89)90733-3.
[14] P.M.G. Nambissan, P. Sen, Positron annihilation study of the annealing behaviour of alpha induced defects in tungsten, Radiat. Eff. Defect Solid 124 (1992) 215, https://doi.org/10.1080/10420159208220193.
[15] A. Debelle, M.F. Barthe, T. Sauvage, First temperature stage evolution of irradiation-induced defects in tungsten studied by positron annihilation spectroscopy, J. Nucl. Mater. 376 (2008) 216, https://doi.org/10.1016/j.jnucmat.2008.03.002.
[16] O.V. Ogorodnikova, L.Y. Dubov, S.V. Stepanov, D. Terentyev, Y.V. Funtikov, Y.V. Shtotsky, V.S. Stolbunov, V. Efimov, K. Gutorov, Annealing of radiation-induced defects in tungsten: positron annihilation spectroscopy study, J. Nucl. Mater. 517 (2019) 148, https://doi.org/10.1016/j.jnucmat.2019.02.010.
[17] L. Cheng, Z.H. Zhao, G.D. Temmerman, Y. Yuan, T.W. Morgan, L.P. Guo, B. Wang, Y. Zhang, B.Y. Wang, P. Zhang, X.Z. Cao, G.H. Lu, Effect of noble gas ion pre-irradiation on deuterium retention in tungsten, Phys. Scripta T167 (2015), 014001, https://doi.org/10.1088/0031-8949/2015/T167/014001.
[18] X.-L. Zhu, Y. Zhang, L. Cheng, Y. Yuan, G.D. Temmerman, B.-Y. Wang, X.-Z. Cao, G.-H. Lu, Deuterium occupation of vacancy-type defects in argon-damaged tungsten exposed to high flux and low energy deuterium plasma, Nucl. Fusion 56 (2016), 036010, https://doi.org/10.1088/0029-5515/56/3/036010.
[19] A.M. Ito, A. Takayama, Y. Oda, T. Tamura, R. Kobayashi, T. Hattori, S. Ogata, N. Ohno, S. Kajita, M. Yajima, Y. Noiri, Y. Yoshimoto, S. Saito, S. Takamura, T. Murashima, M. Miyamoto, H. Nakamura, Hybrid simulation research on formation mechanism of tungsten nanostructure induced by helium plasma irradiation, J. Nucl. Mater. 463 (2015) 109, https://doi.org/10.1016/j.jnucmat.2015.01.018.
[20] A. Yabuuchi, N. Oshima, H. Kato, B.E. O'Rourke, A. Kinomura, T. Ohdaira, Y. Kobayashi, R. Suzuki, Annealing of a pre-assembled tungsten positron moderator by direct electron bombardment, JJAP Conf. Proc. 2 (2014), 011102, https://doi.org/10.7567/JJAPCP.2.011102.
[21] Primary Radiation Damage in Materials, The OECD Nuclear Energy Agency, 2015, p. 34.
[22] J.F. Ziegler, SRIM-2003, Nucl. Instrum. Methods Phys. Res., Sect. B 219–220 (2004) 1027, https://doi.org/10.1016/j.nimb.2004.01.208.
[23] J.F. Ziegler, M.D. Ziegler, J.P. Biersack, SRIM—the stopping and range of ions in matter (2010), Nucl. Instrum. Methods Phys. Res., Sect. B 268 (2010) 1818, https://doi.org/10.1016/j.nimb.2010.02.091.
[24] P.J. Schultz, K.G. Lynn, Interaction of positron beams with surfaces, thin films, and interfaces, Rev. Mod. Phys. 60 (1988) 701, https://doi.org/10.1103/RevModPhys.60.701.
[25] Q. Xu, K. Sato, T. Yoshiie, T. Sano, H. Kawabe, Y. Nagai, K. Nagumo, K. Inoue, T. Toyama, N. Oshima, A. Kinomura, Y. Shirai, Positron beam facility at Kyoto University research reactor, J. Phys.: Conf. Ser. 505 (2014), 012030, https://doi.org/10.1088/1742-6596/505/1/012030.
[26] K. Sato, Q. Xu, T. Yoshiie, T. Sano, H. Kawabe, Y. Nagai, K. Nagumo, K. Inoue, T. Toyama, N. Oshima, A. Kinomura, Y. Shirai, Development of a mono-energetic positron beam line at the Kyoto university research reactor, Nucl. Instrum. Methods Phys. Res., Sect. B 342 (2015) 104, https://doi.org/10.1016/j.nimb.2014.09.022.
[27] A. Yabuuchi, R. Naka, K. Sato, Q. Xu, A. Kinomura, Slow-positron beamline temperature rise reduction at Kyoto university research reactor, Nucl. Instrum. Methods Phys. Res., Sect. B 461 (2019) 137, https://doi.org/10.1016/j.nimb.2019.09.036.
[28] A. Yabuuchi, T. Yoshiie, A. Kinomura, Contribution of cadmium to the total amount of positron creation in a reactor-based slow positron beamline, Nucl. Instrum. Methods Phys. Res., Sect. B 463 (2020) 40, https://doi.org/10.1016/j.nimb.2019.11.028.
[29] M.J. Caturla, T.D. de la Rubia, M. Victoria, R.K. Corzine, M.R. James, G.A. Greene, Multiscale modeling of radiation damage: applications to damage production by GeV proton irradiation of Cu and W, and pulsed irradiation effects in Cu and Fe, J. Nucl. Mater. 296 (2001) 90, https://doi.org/10.1016/S0022-3115(01)00569-4.
[30] T. Troev, N. Nankov, T. Yoshiie, Simulation of displacement cascades in tungsten irradiated by fusion neutrons, Nucl. Instrum. Methods Phys. Res., Sect. B 269 (2011) 566, https://doi.org/10.1016/j.nimb.2011.01.010.
[31] R.S. Averback, Atomic displacement processes in irradiated metals, J. Nucl. Mater. 216 (1994) 49, https://doi.org/10.1016/0022-3115(94)90006-X.